ANNUAL REVIEWS

Annual Review of Condensed Matter Physics

Brittle Fracture Theory Describes the Onset of Frictional Motion

Ilya Svetlizky, Elsa Bayart, and Jay Fineberg

The Racah Institute of Physics, The Hebrew University of Jerusalem, Jerusalem 91904, Israel; email: jay@mail.huji.ac.il

Annu. Rev. Condens. Matter Phys. 2019. 10:253–73

First published as a Review in Advance on December 10, 2018

The *Annual Review of Condensed Matter Physics* is online at conmatphys.annualreviews.org

https://doi.org/10.1146/annurev-conmatphys-031218-013327

Keywords

friction, fracture mechanics, rupture fronts

Abstract

Contacting bodies subjected to sufficiently large applied shear will undergo frictional sliding. The onset of this motion is mediated by dynamically propagating fronts, akin to earthquakes, that rupture the discrete contacts that form the interface separating the bodies. Macroscopic motion commences only after these ruptures have traversed the entire interface. Comparison of measured rupture dynamics with the detailed predictions of fracture mechanics reveals that the propagation dynamics, dissipative properties, radiation, and arrest of these "laboratory earthquakes" are in excellent quantitative agreement with the predictions of the theory of brittle fracture. Thus, interface fracture replaces the idea of a characteristic static friction coefficient as a description of the onset of friction. This fracture-based description of friction additionally provides a fundamental description of earthquake dynamics and arrest.

1. INTRODUCTION

Frictional resistance has puzzled mankind for thousands of years. One reason is its enormous importance. Frictional forces will stop our cars—as well as keep them on the road. Extensive efforts have been directed toward understanding friction across scales, from single nanometric contacts (1–3) to natural faults and earthquakes (4–7). Although descriptions of friction date back to at least the early Egyptians (8, 9), the foundations for the modern study of friction were laid by Leonardo da Vinci, whose early experiments suggested that the onset of frictional motion is predicted by the ratio of shear to normal forces acting on contacting bodies. The simplicity of this description has been challenged by recent experiments. Detailed measurements have revealed that the onset of sliding is mediated by complex spatiotemporal dynamics that take place at the contacting interface that separates sliding bodies. Motion is initiated when the ensemble of micro-contacts, which make up a rough frictional interface, are broken by means of propagating rupture fronts. These rupture fronts, which are akin to earthquakes, may approach the speed of sound. Macroscopic sliding of two bodies commences only after such a front has traversed the entire frictional interface. These rupture fronts, which can be mapped to cracks, couple dynamics at time and length scales that are separated by many orders of magnitude. The interplay of these is the key to understanding friction.

This review focuses on the dynamics of frictional rupture fronts at the onset of motion. Our aim is to both show how the friction problem is related to the fracture dynamics and present experimental evidence that validates this "fracture mechanics" framework. To this end, we intentionally omit numerous important topics in the study of friction such as contact mechanics and effects of roughness (10–16), wear (17), microscopic models of frictional interfaces (8, 18, 19), and stability of frictional sliding (18, 20, 21). Furthermore, we simplify our discussion to sub-Rayleigh rupture fronts propagating along an interface separating identical materials. We therefore do not include in this review recent contributions in our understanding of supershear ruptures and rupture propagating along bimaterial interfaces. The structure of this review is as follows: After briefly reviewing single degree of freedom descriptions of friction, we sketch, in Section 2.1, the fracture mechanics theoretical framework that replaces this simplistic view of friction when the spatial degrees of freedom along an extended frictional interface are properly accounted for. After demonstrating that the elastic fields at the tip of propagating ruptures are very well described by the universal singular solutions originally developed to describe brittle shear cracks (Section 2.1), we show that the classical equation of motion derived for brittle shear cracks perfectly describes the acceleration (Section 2.2) and arrest (Section 2.3) of frictional ruptures (laboratory earthquakes). Furthermore, we demonstrate how this quantitative framework can be used to explore the elusive properties of both the hitherto hidden interface. In Section 2.4, we demonstrate how nonsingular contributions capture the unique form of stress-wave radiation resulting from rapid rupture acceleration. Finally, we discuss how the singular fields at a rupture tip are regularized (Section 2.5).

1.1. Single Degree of Freedom Representation of Friction

Let us consider two contacting bodies that are pressed together by an external normal force F_N and subjected to a slowly increasing shear loading (**Figure 1*a***, *top*). This system eventually undergoes slip-stick motion, i.e., alternating start-stop motion. In the stick phase, the interface separating the two bodies resists the relative motion of the bodies and F_S increases slowly with the applied loading. At the onset of motion, F_S rapidly decreases as the relative motion (slip) of the blocks commences; the sliding bodies accelerate away from the points where F_S is applied (**Figure 1*b***), reducing its value rapidly. Typically, frictional resistance at the onset of motion is larger than the resistance during sustained sliding. Both are commonly thought to be proportional to the applied normal force where the proportionality factors, μ_s and μ_d, are respectively defined as the static and

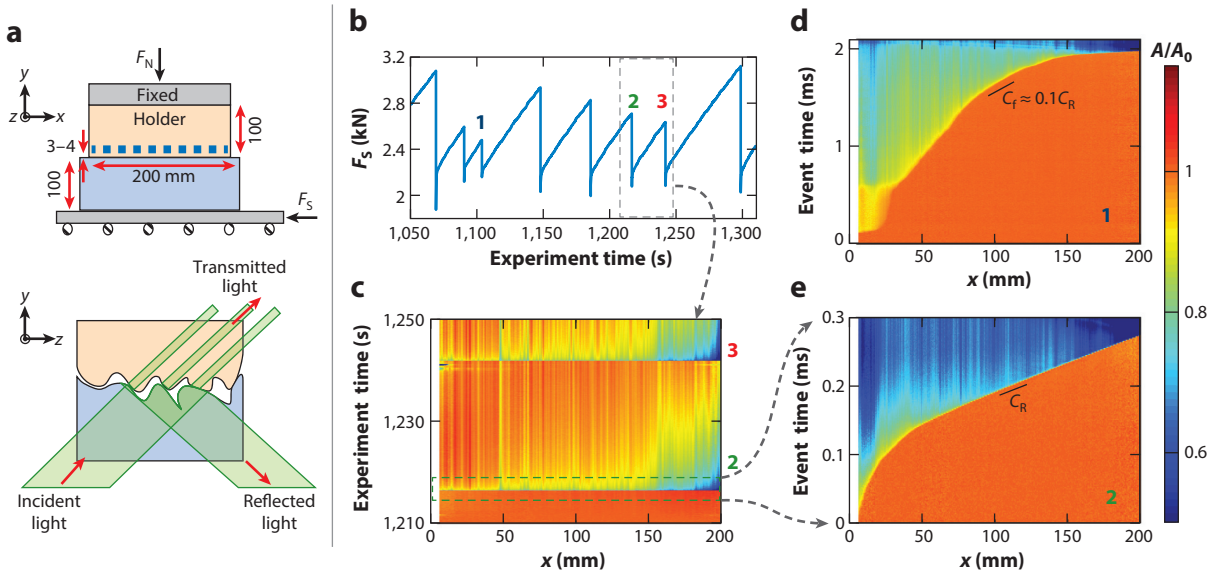

Figure 1

Stick-slip motion is mediated by propagating rupture fronts. (*a*) Experimental system. Two PMMA plates are pressed together with a normal force F_N. The real area of contact $A(x,t)$ along the 200-mm quasi-one-dimensional interface is measured by a method of total internal reflection (*bottom*) (44) at a rate of 580,000 frames per second and averaged along the z direction. In parallel, the complete two-dimensional strain tensor,ε_{ij}, is measured along and slightly above the frictional interface at 1,000,000 samples per second at 14–19 points along the interface (*blue squares* in panel *a*, *top*). (*b*) A shear force F_S is quasi-statically incremented during the stick phase ($F_N \approx 5{,}500$ N, and its variation is negligible). The onset of motion is characterized by rapid drops in F_S and (*c*) a rapid reduction of $A(x,t)$. Note that the events labeled 1, 2, and 3 in panel *b* correspond to those described in panels *c*, *d*, and *e*. In the times between events, A reheals because of aging (31, 32), and the interface regains its strength. In panel *c*, $A(x,t)$ was normalized at the nucleation time of event 2. Color bar is provided on the far right. (*d*,*e*) Typical examples of the short time evolution of $A(x,t)$ (normalized by $A_0 = A(x, t_{nuc})$ at the time t_{nuc} at which the nucleation of each event occurred) for a (*d*) slow and (*e*) fast rupture front. Here, all ruptures nucleated at $x \approx 0$ and accelerated while propagating in the positive x direction. For PMMA, $C_R \approx 1237$ m/s. Panels *d* and *e* taken from References 145 and 86, respectively. Abbreviation: PMMA, poly(methylmethacrylate).

dynamic friction coefficients. In this rather simple description, typically referred to as Amontons–Coulomb friction laws, friction coefficients depend solely on the material properties, which are independent of the loading configuration, the geometry of the bodies, and the nominal area of the frictional interface.

In the 1950s, Bowden & Tabor (22) laid the foundations for understanding Amontons–Coulomb friction laws. They realized that the real area of contact A formed by rough contacting surfaces is substantially smaller than the nominal contact area, A_{nom}, as it is composed of myriad discrete microscopic contacts (**Figure 1*a***, *bottom*). The applied nominal normal pressure, $\sigma = F_N/A_{nom}$, is balanced by the mean pressure at these contacts. The real pressure at these contacts is therefore huge, F_N/A, often reaching the material hardness, σ_H. If an ideal plastic model is considered, one expects that

$$A/A_{nom} \sim \sigma/\sigma_H, \qquad 1.$$

as was demonstrated for some transparent materials (23). The proportionality between A and σ is not, however, unique to situations in which the touching asperities deform plasticly and may occur even under fully elastic deformation if a reasonable distribution of the asperities height and radius is taken into account (10).

In the next step, frictional resistance per nominal unit area τ is related to the shear strength of the microcontacts τ_s by

$$\tau = \tau_s \cdot A/A_{nom}. \qquad 2.$$

By combining both equations, we get $\mu_s = \tau_s/\sigma_H$, which encapsulates the salient features of Amontons–Coulomb friction.

There have been a number of modifications to the Amontons–Coulomb friction laws. For completeness, we briefly mention some of these. Pioneering experiments by Rabinowicz (24) revealed two significant corrections: healing and slip rate dependence. μ_s was shown to increase logarithmically with time when surfaces are held in stationary contact under applied normal load. This "healing" enables the static friction to recover from its lower dynamic value attained during sliding. Slip rate dependence characterized by logarithmic velocity weakening of μ_d for steady sliding was also observed for slow slip velocities $v < 1$ mm/s. Finally, the transition between one value of friction to another was found to be accompanied by a critical slip distance. This phenomenology is rather general and has been observed for metals (24), rock (6, 25, 26), and polymer glasses (18, 27, 28).

All this phenomenology can be incorporated in rate-and-state formulations of friction. The starting points are Equations 1 and 2, where an instantaneous rate dependence of the microcontact shear strength, $\tau_s = \tau_s(v)$, is introduced. Generally, $\tau_s(v)$ is an increasing function of v (29). The history dependence and the evolution of the contact area are given by $A(\phi)$, where ϕ is defined as a state variable that is typically interpreted as the contact life time. Setting $\phi = t$, for instance, captures the logarithmic increase of A with contact time (aging) of pressed materials (30–32), and therefore describes the healing of μ_s (27). Note, however, that recent experiments indicate that A exhibits rich healing effects that cannot be fully captured by a single state variable (33). Extensive efforts have been invested in formulating evolution laws for ϕ that typically have the form $\dot{\phi} = f(\phi, v)$ (6, 32, 34, 35). Evolution laws are necessary to capture the time and slip history of both the evolution of friction with v as well as the dynamics of interface healing.

Typically, the above corrections to Amontons–Coulomb friction are small and are observed for conditions of low slip rates ($v < 1$ mm/s) and modest displacements (<1 cm). At these rates, the heat generated at the contacts can diffuse away appreciably over a contact lifetime (d_c/v, where d_c is a typical contact size), resulting in a rather small temperature increase. Motivated by the high seismic slip rates characteristic of large earthquakes, rotary shear apparatuses have recently tested much higher slip rates (~1 m/s). At sufficiently high slip rates, experiments in rock have demonstrated extreme reductions of the frictional resistance. These have been associated with a variety of different mechanisms that include flash heating (local melting) of the contacts (36–38), powder lubrication (39, 40) of the ground rock (gouge) that is trapped within the frictional interfaces, triggering of mechanically and thermally activated chemical reactions (41), and eventually, melting (42). For an extensive review of this class of experiments, see Di-Toro et al. (43).

1.2. Spatiotemporal Dynamics at the Onset of Frictional Motion

The underlying premise in the friction studies previously discussed is that the sliding bodies are entirely rigid. Hence, their spatial degrees of freedom can be neglected, and their relative motion can be represented by a single degree of freedom. The combined stiffness of the experimental apparatus and the elasticity of the bodies surrounding the interface, in this view, is often modeled by a single effective "spring." The applied shear force (deformation of the spring) essentially provides a measure of the friction force, if inertia is neglected.

In realistic cases, however, these assumptions are not satisfied, and frictional motion entails rich and complex spatiotemporal dynamics. One such example is the onset of frictional motion. As materials are both flexible and deformable, rather than rigid, it is not realistic to assume that sliding will initiate along the entire frictional interface instantaneously and simultaneously at each contacting point. Instead, motion (slip) initiates locally, and overall sliding of the bodies commences only after propagating crack-like rupture fronts, which separate the sticking and sliding spatial regions, traverse the interface. **Figure 1*d*,*e*** presents typical examples of both slowly ($C_f \sim 0.1C_R$) and rapidly ($C_f \sim C_R$) propagating ruptures, respectively, where C_f and C_R are, respectively, the speed of the fronts and the Rayleigh wave speed (the asymptotic velocity of singular shear cracks). The propagating fronts are visualized by high-speed spatial measurements of A (44). In these examples, ruptures nucleate at $x \approx 0$, accelerate in the positive x direction, and leave in their wake a significantly reduced A.

Ignoring these rupture fronts by modeling the motion of spatially extended sliding bodies by their center of mass, a single degree of freedom may, therefore, result in erroneous conclusions. Ben-David & Fineberg (45) demonstrated that the macroscopically measured static friction coefficient, $\mu_s = F_S/F_N$, is not only a material constant but also may vary systematically with controlled variation of the external loading configuration. These variations were tightly linked to changes in the rupture dynamics. Furthermore, **Figure 1** demonstrates that μ_s may significantly vary even within the same stick-slip sequence, with lower μ_s values associated with nucleation of slower ruptures. The whole concept of a static friction coefficient is therefore insufficient to determine the onset of global frictional slip. This is exemplified by large reported variations in measurements of μ_s (46) (up to a factor of 2) under ostensibly identical conditions. The criterion for global slip, instead, is intimately related to the question of what determines rupture nucleation.

The importance of the spatiotemporal dynamics of these rapidly propagating fronts is further highlighted if one considers the hundreds of kilometers-long natural faults that separate tectonic plates. The slow motion of tectonic plates over hundreds of years results in a gradual increase of their stored elastic energy. The release of this energy occurs through rapidly propagating rupture fronts that generate the strong ground motion that we equate with earthquakes (4). The intimate relationship between earthquakes and laboratory stick-slip instability, as was recognized by Brace & Byerlee (47), has triggered extensive experimental studies of crack-like dynamics along frictional interfaces (7, 48–51).

2. FRICTIONAL RUPTURE FRONTS: EXPERIMENTS AND MODELING

2.1. Singular Elastic Fields Drive Frictional Rupture Fronts

We now show that the rupture fronts, such as those described in **Figure 1**, are essentially shear cracks. We limit our discussion to sub-Rayleigh ruptures ($C_f < C_R$) that propagate within an interface separating identical materials. To proceed, we first briefly review the basic concepts of linear elastic fracture mechanics (LEFM), the theoretical framework that describes crack propagation. The dynamic behavior of deformed linearly elastic materials can be described by two wave equations, one for longitudinal waves (with a characteristic wave speed C_L) and one for shear waves (with characteristic wave speed C_S) (52, 53). Mathematically, a propagating crack in a two-dimensional solid (see **Figure 2*a***) is introduced by traction-free boundary conditions at the crack faces, i.e., $\sigma_{xy} = \sigma_{yy} = 0$. These boundary conditions essentially couple both wave equations. The in-plane opening mode of tensile crack deformation (mode I, σ_{yy}), the in-plane shearing mode (mode II, σ_{xy}), and the antiplane shearing mode (mode III, σ_{yz}) can be treated separately. Solving the complete time-dependent boundary value problem is a formidable task. A solution for a steadily moving crack, propagating at speeds below C_S, can be obtained, however, in the form of

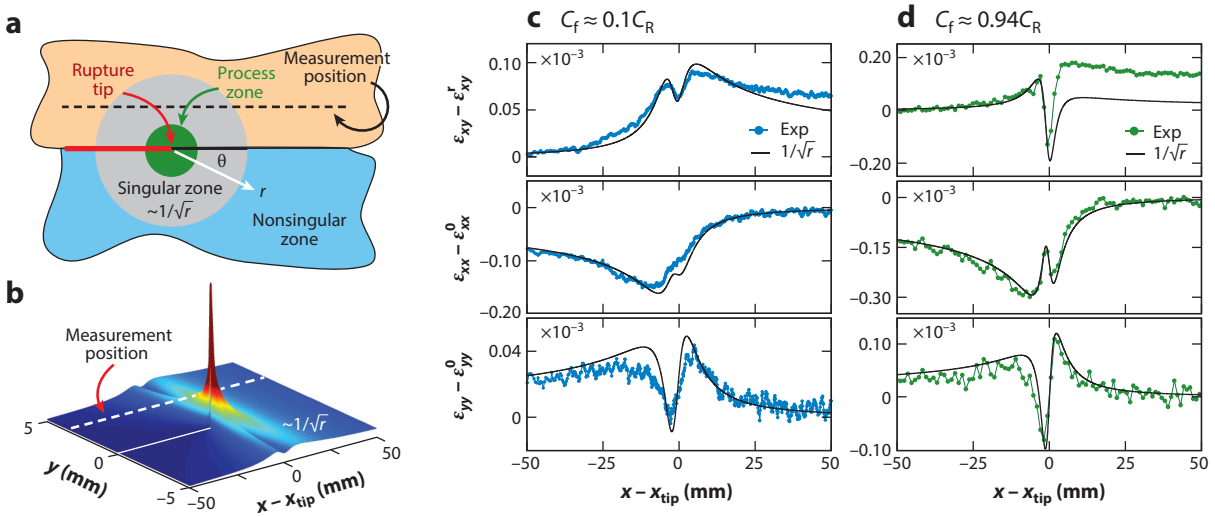

Figure 2

The $1/\sqrt{r}$ form of the elastic strains. (*a*) Stresses at the vicinity of the crack tip have a universal $1/\sqrt{r}$ singular form (*gray region*). Singular stresses are regularized in the process zone (*green region*), where dissipation takes place. Nonsingular contributions should be taken into account at distances from the crack tip where they become comparable with the singular contribution. (*b*) The calculated shear strain ε_{xy} surrounding the rupture tip predicted by Equation 5 for $C_f = 0.1C_R$. The white dashed line corresponds to the strain measurement location relative to the frictional interface $y = 0$. Note the angular dependence that drives the rapid oscillations evident in the measurements presented in panels *c* and *d*. Measurements of strain tensor variations, ε_{ij}, slightly above the frictional interface ($y = 4$ mm), for (*c*) a slowly propagating rupture ($C_f \approx 0.1C_R$) and (*d*) a rapid rupture ($C_f \approx 0.94C_R$). These measurements were acquired during the rupture events presented in **Figure 1*d*,*e***. The corresponding LEFM predictions of Equation 5 are plotted in black. Here, both measurements were performed for the same normal load but for different values of the imposed shear. In both, $\Gamma \approx 2.5$ J/m^2 is the sole free parameter. ε^r_{xy}, ε^0_{xx}, and ε^0_{yy} are, respectively, the residual shear strain after passage of the fronts and the initial values of the strain tensor in the propagation and normal directions. Data taken from Reference 86. Abbreviation: LEFM, linear elastic fracture mechanics.

an asymptotic expansion in powers of $r^{n/2}$, where r is the distance from the crack tip and n is an integer. In the close vicinity of a crack tip, stresses are described by a singular term (with integrable energy) that dominates nonsingular contributions,

$$\sigma_{ij} = \sum_{\alpha=\mathrm{I,II,III}} \frac{K_\alpha}{\sqrt{2\pi r}} \Sigma^\alpha_{ij}(\theta, C_f), \qquad 3.$$

where (r, θ) are polar coordinates with respect to the crack tip. Σ^α_{ij} are known universal functions. Here, α labels the different fracture modes, and C_f is the instantaneous crack velocity. The scalar quantities K_α are commonly called the stress intensity factors. K_α are determined by the outer boundary conditions (loading conditions) as well as the crack's profile: length l, history, and instantaneous dynamics (52). σ_{ij} are linearly related to the strain field ε_{ij} via Hook's law $\sigma_{ij} = 2\mu[\varepsilon_{ij} + (1/2k^2 - 1)\varepsilon_{ll}\delta_{ij}]$, where μ is the shear modulus and $k = C_S/C_L$(53). This square-root singularity of the elastic fields, which essentially defines brittle fracture, is universal in the sense that its form does not depend on the geometry and outer boundary conditions.

It is interesting that shear-driven (mode II) fracture is generally considered to be impossible in bulk isotropic materials because it is believed that a crack will rotate under imposed shear so as to fracture under pure tension (54). The highly anisotropic conditions, embodied in the case of the weak interface plane that defines a frictional interface, constrain the crack to this plane and thereby provide one case where mode II fracture may indeed be realized. This important case is

the focus of this review. The problem of crack path selection, one of the major unsolved fracture mechanics problems, is circumvented here because only mode II straight cracks are considered.

With the elastic fields in hand, the energy flux through any closed contour surrounding the crack tip can be calculated. It can be shown that within the singular region (where the K fields dominate), K_{II} determines the energy flux per unit crack advance, G_{II}:

$$G_{\mathrm{II}} = \frac{K_{\mathrm{II}}^2}{4\mu(1-k^2)} f_{\mathrm{II}}(C_{\mathrm{f}}, k), \qquad 4.$$

where $f_{\mathrm{II}}(C_{\mathrm{f}}, k)$ is a known function (52, 53) that is fairly constant for low velocities and diverges as C_{f} approaches the Rayleigh wave speed, C_{R} (note that $C_{\mathrm{R}} < C_{\mathrm{S}}$). C_{R} is the limiting value of C_{f} so long as the point singularity embodied in Equation 3 holds (see Section 2.2).

The fracture energy Γ is defined as the energy dissipated per unit of newly created surface area. Γ incorporates all unknown dissipation mechanisms. Its calculation from first principles is very challenging, and thus one relies on experimental measurements to determine its value. For a crack to propagate, the elastic energy flowing into the crack tip must equal the energy dissipated by creating new surface. Hence, the energy balance condition $\Gamma = G_{\mathrm{II}}$ must hold.

A crucial difference exists between real cracks and frictional ruptures. Whereas crack faces are stress free (the material is broken), within the wake of frictional ruptures the bodies are always in partial contact [$\sigma_{yy}^0(x) \neq 0$], and the frictional resistance, $\tau_r(x)$, opposes sliding. Using the linearity of the governing equations, however, the problem of a frictional rupture front, propagating within an interface separating identical materials, can be mapped to the stress-free conditions that define the mode II crack problem (55). Thus, stresses in the vicinity of a frictional rupture tip are therefore predicted to be

$$\sigma_{ij} = \frac{K_{\mathrm{II}}}{\sqrt{2\pi r}} \Sigma_{ij}^{\mathrm{II}}(\theta, C_{\mathrm{f}}) + \begin{bmatrix} \sigma_{xx}^0 & \tau_{\mathrm{r}} \\ \tau_{\mathrm{r}} & \sigma_{yy}^0 \end{bmatrix}. \qquad 5.$$

Note, however, that when friction depends on the sliding velocity, for example, linear viscous friction, a new form of singularity may emerge (56). We also note that ruptures propagating along (bimaterial) interfaces that separate bodies with different elastic properties (57–61) have different dynamics.

The infinite stresses at the rupture tip are naturally regularized in some vicinity of the rupture tip, which is called the process or cohesive zone. The region in which the square-root singular form dominates, therefore, should be interpreted as an intermediate asymptotic' region separating the inner scales of dissipation from the outer region where nonsingular contributions cannot be neglected (**Figure 2*a***). This assumption is typically coined "small scale yielding" (62, p. 380).

Is Equation 5 together with the assumption of small-scale yielding valid for frictional rupture fronts? Recent experiments (63) have shed light on this question. The complete 2D strain tensor ε_{ij} was measured slightly above the frictional interface formed by two acrylic [poly(methylmethacrylate) or PMMA] plates (see **Figures 1*a*** and **2*a***). **Figure 2*c*,*d*** shows measured ε_{ij} for the slow and fast rupture events presented in **Figure 1*d*,*e***, respectively. As C_{f} increases, all ε_{ij} amplitudes grow significantly, and strain oscillations are strongly amplified. Comparison with the square-root singular form predicted by LEFM shows that for slow ruptures all the measured strain components ε_{ij} agree well with the strains corresponding to Equation 5, where the only free parameter used was the value of K_{II}. Because the strain measurements were, necessarily, displaced from the interface, each ε_{ij} measurement involved both radial and angular variations (see **Figure 2*b***). K_{II} is related uniquely to Γ for each C_{f} by using Equation 4 and energy balance $G_{\mathrm{II}} = \Gamma$. These measurements therefore provided the explicit value of Γ at the interface.

Figure 2*d* demonstrates that for the same constant value of Γ nearly all the characteristic features of ε_{ij} observed at higher rupture velocities are also well described by the $1/\sqrt{r}$ form. For example, the violent high-amplitude strain oscillations that occur when the rupture tip passes beneath the measurement point (**Figure 2*b***) are due to the singular nature of $\Sigma_{ij}^{\mathrm{II}}(\theta, C_{\mathrm{f}})$ as $C_{\mathrm{f}} \rightarrow C_{\mathrm{R}}$. In fact, Reference 63 concluded that with a single input value of Γ, the theory quantitatively describes the strain variations throughout the entire sub-Rayleigh velocity range $0.1C_{\mathrm{R}} < C_{\mathrm{f}} < 0.99C_{\mathrm{R}}$. **Figure 2*d*** (*top*), however, shows that Equation 5 clearly fails to describe ε_{xy} ahead of the rupture tip ($x - x_{\mathrm{tip}} > 0$). This apparent discrepancy with the singular solution was shown to be due to nonsingular contributions (65). Its importance is discussed in Section 2.4.

The ability of LEFM to describe the strain fields in the rupture tip vicinity is entirely general. The characteristic signature of the $1/\sqrt{r}$ form (for example, the strong oscillations in ε_{xy} in **Figure 2*d***) have been observed in a variety of different brittle materials: Homalite (figure 4 in Reference 66), granite (figure 1 in Reference 67, figure 10 in Reference 68, and figure 1 in Reference 69), and Indian meta-gabbro (figure 9 in Reference 70).

The generality of LEFM was further demonstrated in Reference 64, in which the onset of motion in the boundary lubrication regime was explored. In this regime, the contacting surfaces are covered by a thin lubricant layer, and the discrete asperities still bear the entire normal load, as they are not entirely immersed in the fluid layer. As in dry friction (**Figures 1** and **2**), each sliding event is preceded by propagating rupture fronts that break the solid contacts forming the interface. **Figure 3*a*** shows explicitly that the strain field variations in the rupture tip vicinity are, again, well described by LEFM. Hence, these ruptures are true brittle shear cracks. Surprisingly, though the lubricated interface reduces the dynamic and static friction relative to the dry interface,

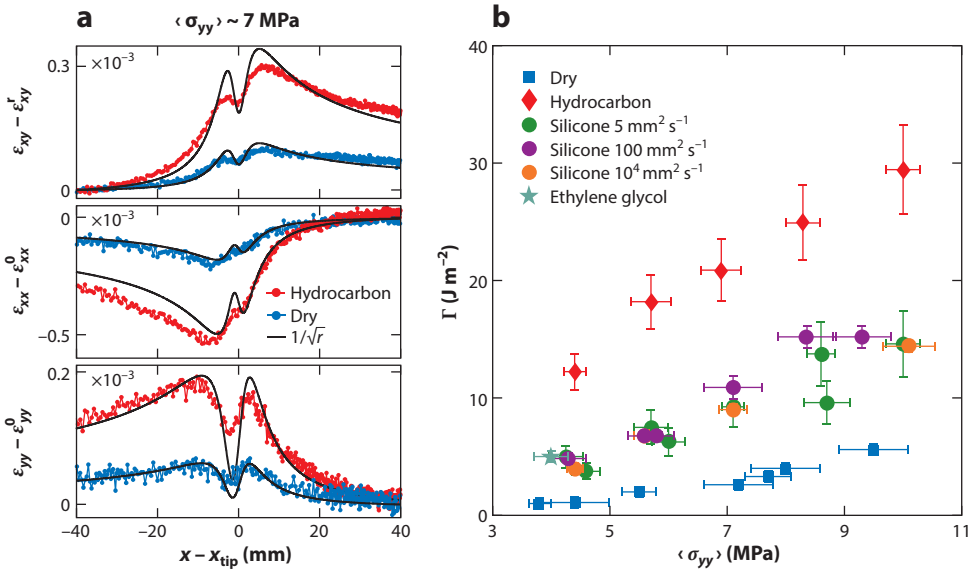

Figure 3

Dependence of the fracture energy with normal stress. (*a*) Comparison of ε_{ij} for ruptures propagating along dry (*blue line*) and boundary-lubricated (*red line*) interfaces. In both, the applied normal stress was $< \sigma_{yy} > \sim 7$ MPa and $C_{\mathrm{f}} \approx 0.3C_{\mathrm{R}}$. Black solid lines are fits to the LEFM solution (Equation 5). The only fitting parameter is the fracture energy; $\Gamma_{\mathrm{dry}} = 2.6 \pm 0.3$ J/m^2 for the dry and $\Gamma_{\mathrm{lub}} = 23 \pm 3$ J/m^2 for the lubricated interfaces. (*b*) Measured values Γ for both the dry and lubricated interfaces versus the normal load. All Γ vary linearly with F_{N}; Γ is independent of the lubricant viscosity while being highly dependent on lubricant composition. Data taken from Reference 64. Abbreviation: LEFM, linear elastic fracture mechanics.

the inferred value of Γ, for the same applied normal load, can be an order of magnitude greater than that for the same nonlubricated interfaces. It is interesting that, as **Figure 3*b*** shows, the values of Γ are independent of the lubricant viscosity, although they are highly dependent on the lubricant's chemical composition.

What determines the value of Γ? Let's first consider dry interfaces. Whereas the bulk fracture energy, Γ_{Bulk}, is a material property (≈2,000 J/m^2 for PMMA), the interface value, Γ, linearly increases with σ_{yy} as shown in **Figure 3*b***. As $\sigma_{yy} \propto A$ (Equation 1), Γ essentially accounts for the change in contact area necessary for a rupture to propagate. In fact, when the sparseness of the contacts (30) ($A \ll A_{\text{nom}}$) was accounted for, the measured values of Γ were indeed found (63) to be consistent with Γ_{Bulk}. This suggests that significant plastic deformation (the major contribution to Γ_{Bulk} in PMMA) should also take place within the contacting asperities.

Why does Γ increase with the addition of a lubricant? The proportionality of Γ in this regime with σ_{yy} (hence A) suggests that the enhancement of Γ by the lubricant layer only takes place at contacts. The enhancement mechanism and its dependence on the chemical composition of the lubricant is both intriguing and not completely understood (64). Although these results are puzzling at the microscopic level, these findings highlight the fact that the fracture mechanics description of frictional motion provides a new way to probe the otherwise hidden and complex dynamics of the all-important interface. Without the microscope that the fracture mechanical analysis of the strength of the frictional layer described in this section provides, we would be entirely blind to the detailed properties of this critical region. This (often) micron-thick layer both possesses wholly different properties than those of the bulk material and determines the strength of the entire macroscopic system.

2.2. Equation of Motion of Frictional Rupture Fronts

How fast can rupture fronts propagate? A wide range of rupture front velocities within laboratory experiments have been observed. These range from slow ruptures (44, 63, 71–73), propagating at a small fraction of the Rayleigh wave speed, C_{R}, to ruptures that asymptotically approach C_{R}. Typical sub-Rayleigh examples are shown in **Figure 1*d*,*e***, and their velocities are plotted in **Figure 4*d***. Under suitable conditions, rupture fronts may also surpass the shear wave speed, C_{S}, and approach the longitudinal speed of sound, C_{L} (38, 65, 72, 74–78).

Experiments by Ben-David et al. (72) first revealed that rupture fronts increase their speed with increased shear to normal stress ratios. Motivated by fracture mechanics, it was suggested that this stress ratio reflects the balance between the potential energy available, prior to rupture, and the energy required to rupture the interface. Later experiments in rock (79), simulations (80–84), and analytical 1D models (85) confirmed these observations.

Once the LEFM predictions (**Figure 2**) for the functional forms of the near-tip stress fields were verified (63), it became possible to test the theory's quantitative predictions for sub-Rayleigh rupture dynamics. These are provided by the energy balance $\Gamma = G_{\text{II}}$ criterion, which provides an implicit equation of motion for shear crack. Quantitative predictions can be made if one is able to explicitly calculate G_{II} or, equivalently, K_{II} (see Equation 4). Such calculations for a general loading configuration are extremely challenging. Freund, in seminal work (52, 87, 88), considered a semi-infinite crack in an unbounded medium subjected to time-independent loading. The crack is initially at rest and then moves at $C_{\text{f}} < C_{\text{R}}$. The stress intensity factor for this type of loading can be explicitly calculated. K_{II} has the following decomposition: $K_{\text{II}}(l, C_{\text{f}}, \Delta\sigma_{xy}) = \kappa_{\text{II}}(C_{\text{f}}) K^{\text{S}}_{\text{II}}(l, \Delta\sigma_{xy})$. Here, $\kappa_{\text{II}}(C_{\text{f}})$ is a known (52) universal dynamic function that depends solely on the instantaneous value of C_{f}. $K^{\text{S}}_{\text{II}}(l, \Delta\sigma_{xy})$, the static/equilibrium stress intensity factor, depends on the instantaneous crack length, l, and incorporates all of the information about the loading through the dynamic

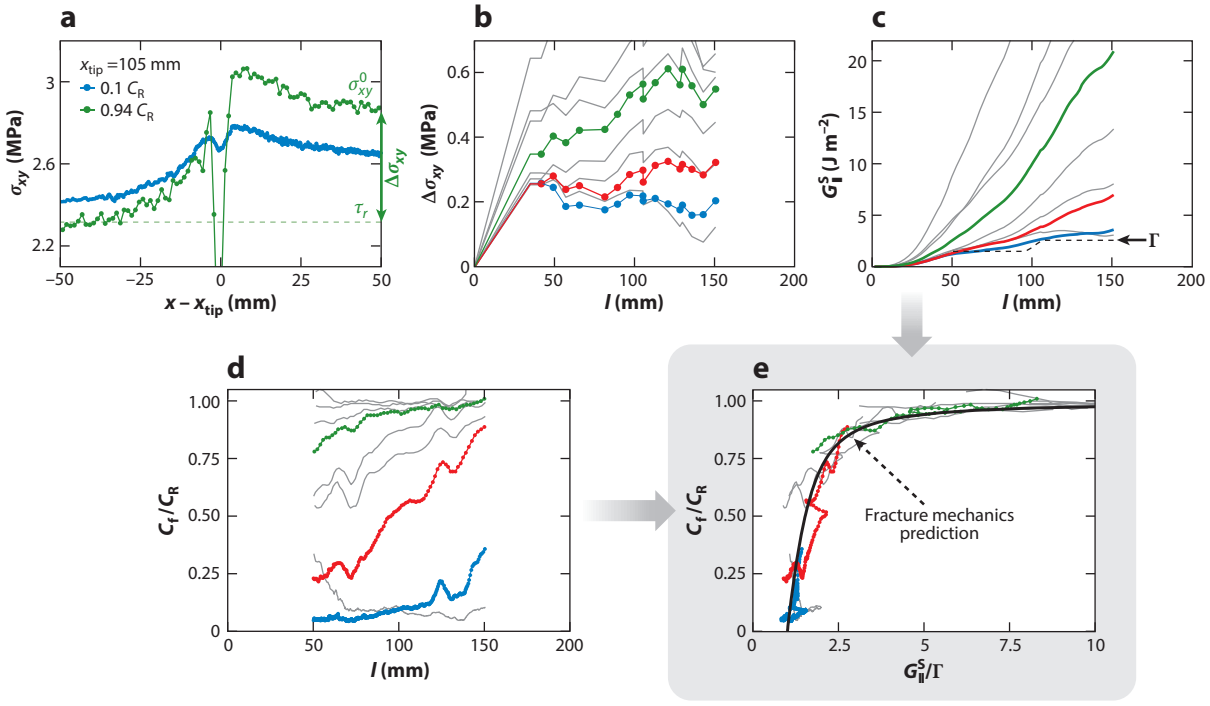

Figure 4

The equation of motion for frictional ruptures. (*a*) Shear stress snapshots, σ_{xy}, calculated from the measured ε_{xy} presented in **Figure 2**. σ^0_{xy} is the initial stress level, prior to the rupture arrival, whereas τ_r denotes the residual stress measured behind the rupture tip. Their difference $\Delta\sigma_{xy} = \sigma^0_{xy} - \tau_r$ defines the dynamic stress drop. (*b*) Measured values of $\Delta\sigma_{xy}$ for a number of different experiments, each with the same value of applied F_N. $\Delta\sigma_{xy}$ near $x = 0$ are extrapolated to $\Delta\sigma_{xy} = 0$ at $x = 0$ with (*d*) their corresponding rupture velocity profiles $C_f(l)$. (*c*) The $\Delta\sigma_{xy}$ profiles in panel *b* yield static energy release rates, $G^S_{II}(l, \Delta\sigma_{xy})$. Dashed line indicates the measured fracture energy profile, $\Gamma(l)$. Slow rupture fronts (*blue line*) are associated with $G^S_{II} \approx \Gamma$ while ruptures rapidly accelerate toward C_R (*green line*) once $G^S_{II} \gg \Gamma$. (*e*) All the $C_f(l)$ profiles collapse to a single functional form $C_f(G^S_{II}/\Gamma)$, given by the classical equation of motion for shear cracks, Equation 6 (*black line*). The blue and green examples correspond to the slow and fast events in **Figures 1*d*,*e*** and **2*c*,*d***. Data taken from Reference 86. Abbreviation: *l*, rupture length.

stress drop, $\Delta\sigma_{xy} = \sigma^0_{xy} - \tau_r$. Here, σ^0_{xy} is the initial stress level, prior to the rupture's arrival, whereas τ_r is the residual frictional resistance (see **Figure 4*a***).

Following Equation 4 and the decomposition of K_{II}, G can now be decomposed into $G_{II} = G^S_{II}(l, \Delta\sigma_{xy})g_{II}(C_f)$, where $G^S_{II}(l, \Delta\sigma_{xy})$, the static energy release rate, can be explicitly calculated once $K^S_{II}(l, \Delta\sigma_{xy})$ is known. For example, under uniformly applied shear, where $\Delta\sigma_{xy}$ is independent of x, G^S_{II} is an increasing function of the crack length: $G^S_{II} \propto (\Delta\sigma_{xy})^2 l/\mu$. The dynamic correction to the energy flux is given by $g_{II}(C_f)$, a universal monotonically decreasing function of C_f that is unity at the limit $C_f \to 0$ and zero at $C_f = C_R$ (see Reference 52 for details). Under these conditions, the equation of motion, $C_f(l)$, for arbitrary stress configurations is implicitly given by

$$\Gamma = G_{II} = G^S_{II}(l, \Delta\sigma_{xy})g_{II}(C_f). \qquad 6.$$

Two main consequences can be directly deduced from Equation 6 and the properties of $g_{II}(C_f)$. (*a*) Crack propagation is energetically possible if and only if $G^S_{II}(l, \Delta\sigma_{xy}) \geq \Gamma$. In particular, under uniformly applied shear, crack propagation is possible only above a critical crack length, termed the Griffith length, $l_c \sim \mu\Gamma/(\Delta\sigma_{xy})^2$. (*b*) C_R is the limiting crack velocity, which can only be reached

asymptotically when $G_{\mathrm{II}}^{\mathrm{S}}(l, \Delta\sigma_{xy}) \rightarrow \infty$. In particular, under these conditions, cracks will accelerate asymptotically to C_{R} as $l \rightarrow \infty$.

In Reference 86 a quantitative test of Equation 6 was conducted for both unlubricated (dry) and boundary-lubricated interfaces. These results are shown in **Figure 4**. **Figure 4*c*** presents the measured profiles of Γ together with the profiles of $G_{\mathrm{II}}^{\mathrm{S}}(l, \Delta\sigma_{xy})$ that were calculated using the measured fields $\Delta\sigma_{xy}(x)$ shown in **Figure 4*b***. Note that while Γ was obtained by direct measurement of the dynamic singular fields (in the near-field) at the rupture tip, $G_{\mathrm{II}}^{\mathrm{S}}$ was calculated using solely the stress drops, $\Delta\sigma_{xy}$, ahead of the rupture tip (far-field stresses). **Figure 4*c,d*** demonstrates that slow ruptures propagate when the static elastic energy released by a unit in advance of the crack is nearly balanced by the dissipated energy, $G_{\mathrm{II}}^{\mathrm{S}} \approx \Gamma$. Loading conditions that result in significant excess elastic energies, $G_{\mathrm{II}}^{\mathrm{S}} \gg \Gamma$, generate rapid acceleration to C_{R}. All of the rupture velocities $C_{\mathrm{f}}(l)$, when plotted with respect to $G_{\mathrm{II}}^{\mathrm{S}}(l, \Delta\sigma_{xy})/\Gamma$, collapse into the precise functional form predicted by Equation 6 (**Figure 4*e***). These experiments explicitly demonstrate that, with no adjustable parameters, the classical equation of motion for brittle shear cracks provides an excellent quantitative description of the velocity evolution of frictional rupture fronts.

Slow ruptures, $C_{\mathrm{f}} \ll C_{\mathrm{R}}$, observed in laboratory experiments, have drawn much recent attention owing to accumulating numbers of observed slow earthquakes (89). In geoscience, slow earthquakes have often been regarded as an entirely different entity than the more traditionally observed rapid ($C_{\mathrm{f}} \sim C_{\mathrm{R}}$) earthquakes. As a result, the driving mechanisms for slow earthquakes are still very much under debate. Slow ruptures have been suggested to emerge as a result of a crossover from velocity-weakening friction at slow slip to velocity-strengthening at higher slip rates (85, 90–92). Alternatively, slow ruptures have been observed in stochastic multiscale simulations (83, 84). Although nontrivial friction laws might well be an important mechanism for stabilizing slow ruptures, measurements such as those presented in **Figure 4** suggest that slow ruptures may simply emerge from any nontrivial stress distribution that would retain a nearly static energy balance defined by $G_{\mathrm{II}}^{\mathrm{S}} \approx \Gamma$ along the propagation path.

The experiments in **Figure 4** describe rupture dynamics that result from a relatively broad range of imposed shear stress levels prior to rupture initiation—hence each took place for very different values of the applied shear force, F_{S} (see **Figure 1*b***). Each of these experiments, however, was performed with the same imposed value of F_{N}. This observation underlines the fact that there is really no characteristic value of μ_{s}. In fact, it was the shear stress at which each rupture nucleated that determined the explicit value of μ_{s}. This stick-slip sequence is an excellent demonstration that frictional interfaces can be either stable or unstable for the same loading conditions, which is in stark contradiction to the picture of frictional onset implied by "single degree of freedom" descriptions of friction described in Section 1.1. Instability of a frictional interface is triggered by the nucleation process—the process by which an initial crack emerges from within a rough interface.

2.3. Rupture Arrest

Frictional ruptures can arrest well before spanning an entire interface. These types of arrested frictional ruptures were first observed in experiments by Rubinstein et al. (94) and a comprehensive review of interface rupture arrest can be found in Reference (95). Here, we briefly describe the main physics of how interface ruptures arrest.

Two typical examples of such arrested ruptures are presented in **Figure 5*c***. Rupture arrest can, for example, result from inhomogeneous stress distributions along the interface. In laboratory experiments, such distributions are often observed if shear forces F_{S} are preferentially applied at one edge of a sample (see **Figure 5*a***, *inset*). Under such loading conditions, a succession of arrested ruptures of increasing lengths are typically observed (e.g., examples A and B in **Figure 5**), well

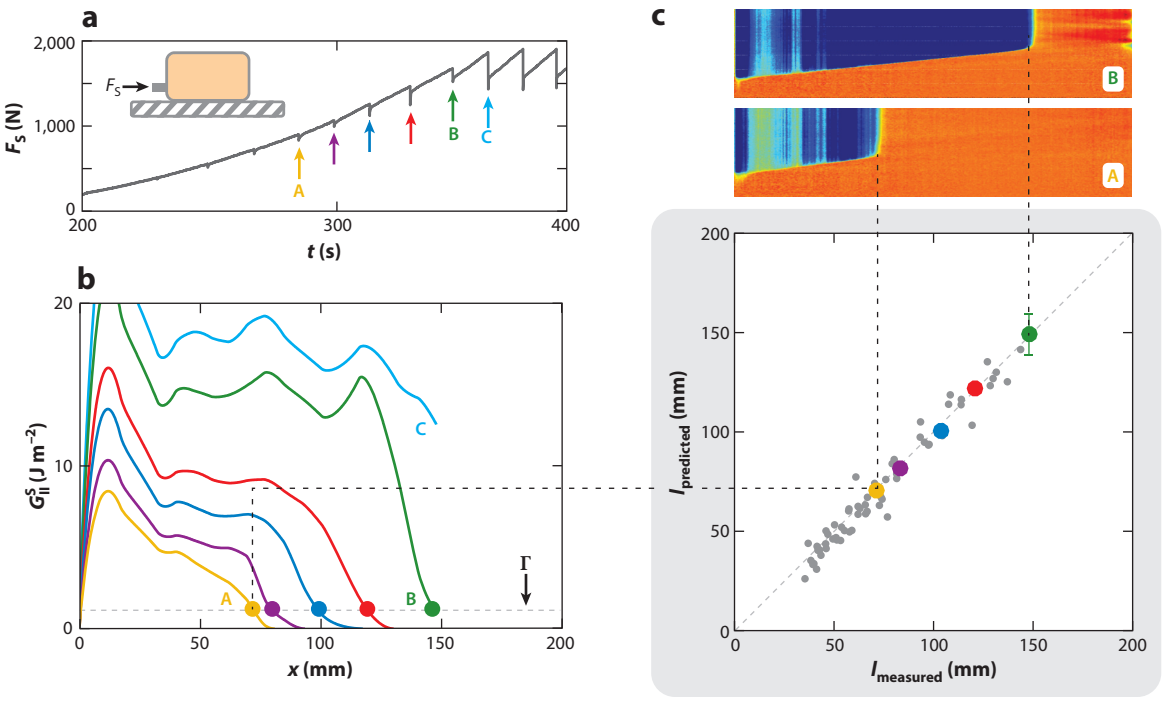

Figure 5

Prediction of rupture arrest locations. (*a*) Loading conditions characterized by F_S applied locally (*inset*) are considered. Well before global sliding (*event C*), a sequence of small force drops are observed. (*b*) The computed static energy release rate G_{II}^S along x for the slip events in panel *a*. Circles denote the predicted location of the arrest, $x = l_{predicted}$, as determined by $G_{II}^S = \Gamma$ (Γ is denoted by the *dashed line*). Note that for event C, the first system-wide sliding event, $G_{II}^S > \Gamma$. (*c*) Comparison of the measured arrested rupture lengths, $l_{measured}$, as determined from the contact area measurements to the predicted lengths, $l_{predicted}$ computed in panel *b*. An additional 12 experiments, each with different normal loads, fracture energies, and stress distributions, are given by the gray dots. The dashed line has a slope of 1. Data taken from Reference 93.

before F_S reaches the threshold for the overall stick-slip motion of the blocks (e.g., example C in **Figure 5**).

Rupture arrest has been observed numerically (82, 96, 97) and a variety of models have been designed to describe the dynamics of precursory ruptures in frictional systems. Aimed at reproducing nucleation and arrest, these include minimalistic one-dimensional (98) and scalar (99) models, discrete contact descriptions (80, 100), and rate-and-state friction laws (101). Although these models were able to reproduce arrested ruptures, they provided no explicit general predictions of where and how arrest occurs in real systems.

Recently, Kammer et al. (102) demonstrated that fracture mechanics can be used to predict the rupture arrest locations observed in Reference 94. In the LEFM framework, crack arrest takes place if the energy flux to the tip of a quasi-statically propagating crack (see discussion in Section 2.2) is insufficient to overcome the fracture energy; $G_{II}^S(l, \Delta\sigma_{xy}) < \Gamma$. This criterion for rupture arrest was explicitly verified in experiments (93), in which a number of different loading conditions and system geometries were considered. In these experiments there were no free parameters; the experimental ingredients required by Equation 6, Γ and $G_{II}^S(l, \Delta\sigma_{xy})$, were either directly measured or calculated by means of direct measurements of $\Delta\sigma_{xy}(l)$. Calculated profiles $G_{II}^S(l, \Delta\sigma_{xy})$ for the typical stick-slip sequence described in **Figure 5*a*** are presented in **Figure 5*b***.

As the figure demonstrates, the predicted arrest locations, $l_{predicted}$, for each event are indeed the precise locations where $G^S_{II}(l, \Delta\sigma_{xy}) < \Gamma$ (see **Figure 5*b*,*c***). **Figure 5*c*** (*bottom*) demonstrates that, in general, $l_{predicted}$ is in excellent agreement with measured arrest lengths, $l_{measured}$, obtained from the contact area measurements.

It is critical to note that though rupture nucleation, as discussed in the previous section, is a necessary condition for the onset of motion, it is insufficient to determine global sliding of the blocks. In this sense, overall frictional slip may occur only if a rupture front reaches the system size, L. Only when $l_{predicted} = L$ will the entire interface be ruptured and will overall slip of the contacting bodies ensue.

Although the results described above are generally relevant for any frictional interface, they are especially important for understanding the essentially unresolved question of what determines the size of an earthquake (103). In fact, fracture mechanics had been used to relate the spatial stress heterogeneities–to–earthquake sizes distribution (104) and recently (105) was successfully implemented to predict the arrest of injection-induced earthquakes. Equation 6 demonstrates that earthquake magnitudes can be determined by the following:

- Nonuniform values of Γ along an interface: At any location where $G^S_{II}(l, \Delta\sigma_{xy}) < \Gamma$, an earthquake should immediately arrest.
- The effects of nonuniform stress profiles: This is an integral effect, as the value of $G^S_{II}(l, \Delta\sigma_{xy})$ is determined by a weighted integral of the stresses $\Delta\sigma_{xy}(l)$ distributed along an interface.

2.4. High-Amplitude Stress-Wave Radiation: Nonsingular Contributions

Nonsteady processes such as the rapid rupture velocity variation during the nucleation or arrest phases have long been suggested to result in the generation of stress-wave radiation (106, 107). In the study of earthquakes, understanding the source mechanism of those waves is of primary importance. Laboratory experiments, therefore, have provided a unique opportunity to shed light on this subject.

A typical example of a rupture front, asymptotically accelerating to rupture velocities, $C_f \to C_R$, is presented in **Figure 6*a***(adapted from Reference 65). **Figure 6*b*** presents measurements of shear stresses, σ_{xy}, at two distinct time steps, t_1 and t_2 (as noted in **Figure 6*a***). Prominent peaks in σ_{xy} precede the rupture tip arrival. Analysis of peak arrival times (see **Figure 6*a***) reveals that they propagate at C_S and, therefore, progressively distance themselves from the rupture tips that created them. Extrapolating the space–time peak trajectories to the intersection point with the rupture trajectory implies that the initiation of this radiated stress wave originates within the latter stages of the accelerating phase.

In crack tip vicinities, all stress (strain) components have the universal $1/\sqrt{r}$ form, as this singular contribution dominates the near-tip stress fields in brittle fracture. These stress peaks, as was mentioned in Section 2.1, are not described by this $1/\sqrt{r}$ form (see **Figure 6*b***). A general description of these radiated stress waves does not exist. Any such analytical description must go beyond the singular contributions to the stress fields. Such full solutions of generally nonsteady dynamic crack problems are extremely difficult to obtain (108). In some simplified cases, however, analytical solutions for accelerating shear cracks are available and have provided much insight (52, 53, 106, 107). One such solution, which was derived both for tension (109) and shear (110), describes bilaterally expanding cracks that initiate with zero initial length and propagate at a constant velocity ($C_f < C_R$) under uniformly applied remote shear stresses (see also References 52 and 53). In this problem, there is no characteristic time or length scale, so self-similar propagating solutions can be found.

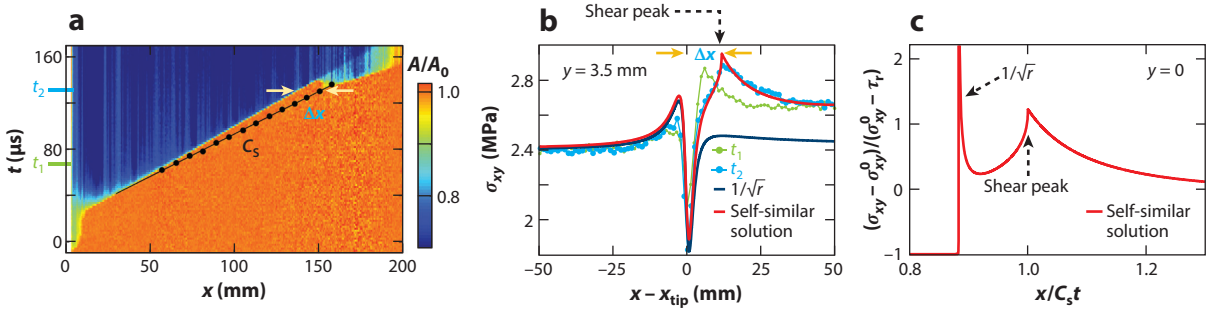

Figure 6

Stress wave radiation of accelerating ruptures. (*a*) $A(x,t)$ evolution (normalized at nucleation time, $t = 0$), along the quasi-1D interface due to a rupture front that nucleated at $x \approx 0$, rapidly accelerated to C_R, and transitioned to supershear at $x \approx 155$ mm. (*b*) σ_{xy} relative to the rupture tip position, x_{tip}, at the two instances, t_1 (*green*) and t_2 (*blue*) denoted in panel *a*, show prominent amplitude shear strain peaks preceding the rupture tip arrival. Successive measurements (*black points* in panel *a*) reveal that these peaks propagate at C_S and trigger supershear rupture. Measurements at t_2 are compared with both the universal $1/\sqrt{r}$ form and the self-similar solution. Although the singular prediction fails at $x - x_{tip} > 0$, the self-similar solution entirely captures the measurements including the initial shear strain σ^0_{xy} and the shear stress peak far before the rupture tip arrival. (*c*) Close-up of the self-similar solution at $y = 0$ shows a pronounced shear stress peak propagating ahead of the singular rupture tip at C_S. Data taken from Reference 65.

The resulting normalized shear stress on the interface ($y = 0$) is plotted in **Figure 6*c***. This solution reveals a singular propagating crack tip that is preceded by a sharp and relatively localized shear stress peak that propagates at C_S. The form and amplitude of this stress peak is generally considered to be an upper bound for the realistic stress-wave radiation of smoothly accelerating ruptures.

Figure 6*b* shows that this self-similar solution of an expanding shear rupture can describe the measured shear stress rather well. In particular, this solution can capture both the initial shear loading, σ^0_{xy}, as well as the propagating shear stress peak far before the rupture tip arrival. This particular solution demonstrates the importance of the nonsingular contributions to strains at finite distances from the rupture front tip (111). Furthermore, the apparent discrepancy with the singular solution (observed in **Figure 6*b*** and **Figure 2*d***, *top*) is not a simple technical issue of accounting for nonsingular contributions to the singular description but actually is a nontrivial radiated wave that possesses a life (and extensive history) of its own. Analytical solutions (106, 107) and accompanying finite element simulations (65) demonstrate that these radiated shear stress peaks have a characteristic near-field signature: high-amplitude radiation (comparable with the dynamic stress drop) that is both localized and strongly focused in the direction of rupture propagation.

The comparison with the self-similar solution highlights the underlying physical picture. Rapid rupture front acceleration (mimicked by the infinite acceleration in the self-similar problem) results in radiation having the form of a localized shear stress peak propagating at C_S. The measurements of $A(x,t)$ presented in **Figure 6*a*** furthermore reveal the sudden nucleation ($x \approx 155$ mm) of a secondary supershear rupture front (propagating at $C_f > C_S$), which surpasses the classic speed limit, C_R, for singular cracks. The synchronized measurements of σ_{xy} and $A(x,t)$ provide direct evidence that the supershear rupture was triggered by the arrival of the shear stress peak. This nucleation mechanism was first postulated in Reference 110. Later numerical work (112) found that a sufficiently strong shear stress peak can overcome interfacial strength and nucleate a daughter crack that could propagate at supershear velocities. Supershear ruptures have been observed along natural fault planes (113, 114) and in laboratory experiments (38, 70, 72, 74–77), and have been extensively investigated by numerical simulations (115–124). A further description, however, is beyond the scope of this review.

2.5. Regularization of the Singular Fields

In the previous section, we briefly described the role of nonsingular far-field contributions to the singular description of LEFM. As we discussed in Section 2.1, the singular $1/\sqrt{r}$ region is interpreted as an intermediate asymptotic: the region that connects the process/cohesive zone in which dissipation takes place to the "outer" region, where nonsingular contributions cannot be neglected (see the schematic view in **Figure 2*a***). In Section 2.1, the "intermediate" $1/\sqrt{r}$ singular region was described. From the singular fields one can directly characterize the interface by means of the fracture energy, Γ. In general, however, very little is known about how the singular fields are regularized within the process zone. How different materials regularize the rupture tip singularities is an interesting and rather important question, as the properties of different materials in this elusive region entirely determine interface strengths. These questions are central to numerous (rather disparate) applications that range from the effects of additives on frictional wear to how natural fault properties affect earthquake dynamics. As interface conditions are extreme, interface properties may have little in common with a material's bulk equilibrium properties (as we saw for the case of boundary layer lubrication).

Regularization of rupture tip singularities is not expected to be universal, as various dissipative processes may take place. Simple models, however, can be used to capture the essential physical mechanisms that take place near the rupture tip. The simplest regularization model was implemented by Barenblatt (125), Dugdale (126), Ida (127), and others, who showed that the singularity of the stress fields can be eliminated by postulating cohesive forces working across the weak plane. In this approach, which is typically termed slip-weakening (55), weakening of the local frictional resistance, τ, is initiated once the shear stress has reached a finite peak strength, τ_p. Subsequently, $\tau(d)$ gradually decreases with the local slip, d, until reaching the dynamic friction level, τ_r. This occurs at a critical slip distance, d_c. The fracture energy is defined as the energy dissipated during weakening, $\Gamma = \int_0^{d_c}[\tau(d) - \tau_r]\mathrm{d}d$. Note that Γ does not account for the dissipation caused by the residual level of friction τ_r. Due to the linearity of the governing equations, subtracting away τ_r (and its associated dissipation) enables the mapping of the friction problem to fracture (see Equation 5).

The simplicity of slip-weakening models makes them extremely useful. They have been extensively used to simulate frictional rupture fronts in a number of contexts that include the supershear transition (118, 120, 128–131), off-fault damage (78, 132, 133), and three-dimensional rupture propagation (134).

Analytically, however, it is often more convenient to use cohesive zone models (55, 135, 136), in which shear stresses gradually decrease from τ_p to τ_r with the spatial position, according to a prescribed spatial stress profile, $\tau(x) = (\tau_p - \tau_r) \cdot \tilde{\tau}(x/x_c) + \tau_r$ (see **Figure 7*a***, *inset*). Here, $x = 0$ is the rupture tip, and x_c is defined to be the cohesive zone size. Small-scale yielding is assumed, and the problem is closed by the universal boundary conditions dictated by the singular K-fields; i.e., far ahead of the crack tip the solution matches the square-root singular form, $\sigma_{xy}(x \gg x_c, y = 0) \rightarrow K_{II}/\sqrt{2\pi x}$ (136). Therefore, $(\tau_p - \tau_r)$, x_c, and Γ are related through Equation 4 and

$$K_{II} = (\tau_p - \tau_r) \cdot \sqrt{x_c} \cdot \sqrt{\frac{2}{\pi}} \cdot \int_{-\infty}^{0} \frac{\tilde{\tau}(\xi)}{\sqrt{-\xi}} \mathrm{d}\xi. \qquad 7.$$

Once the solution is obtained, the equivalent slip-weakening constitutive law, $\tau(d)$, can be calculated.

These models are often criticized as being too simple because they do not take into account the rate and history dependence of the frictional resistance. As discussed in Section 1.1, an intensive

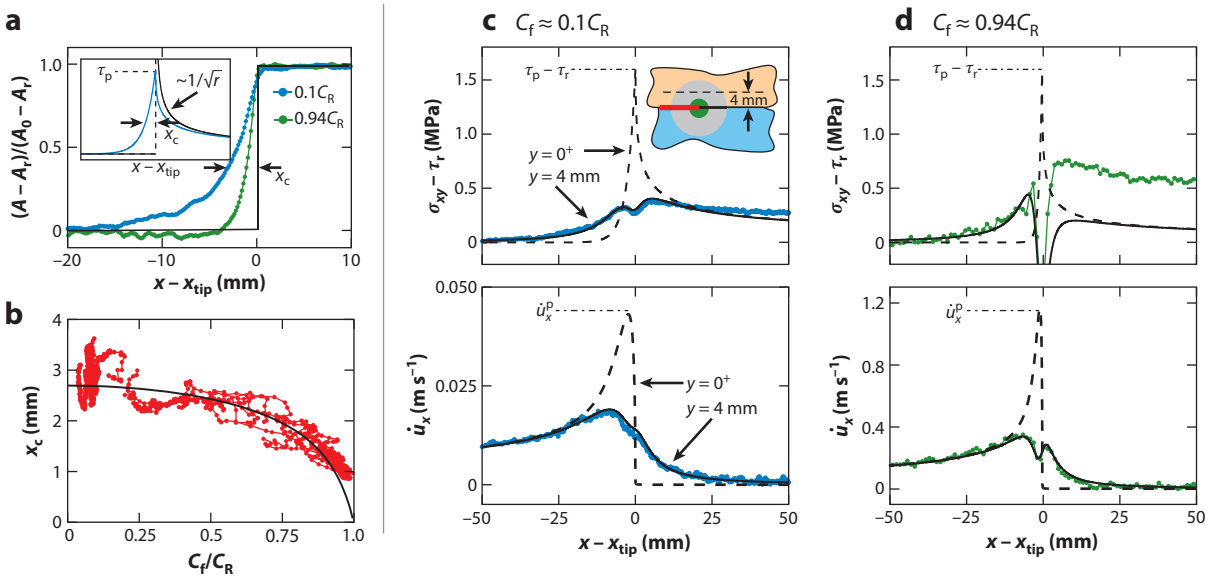

Figure 7

Regularization of the elastic singular fields at the rupture tip. (*a*) The normalized real area of contact, A, is plotted relative to the rupture tip position for the two rupture events described in **Figures 1*d*,*e*** and **2**. A_0 and A_r are the initial (prior to rupture arrival) and residual (after rupture passage) values of A, respectively. x_c is the length scale corresponding to a 60% reduction of A and represents the scale at which the singular fields are regularized. Note the contraction of x_c with increasing C_f. (*a*, *inset*) Schematic drawing of a nonsingular cohesive zone model in which the shear stress is reduced exponentially behind the crack tip once the peak strength, τ_p, is reached (*blue line*). Far ahead of the crack tip the solution matches the square-root singular form (*black line*). (*b*) x_c contracts as $C_f \to C_R$. The black line indicates the linear elastic fracture mechanics prediction. (*c*,*d*) Measurements of the shear stress variation (*top*) and particle velocity $\dot{u}_x = -\varepsilon_{xx} C_f$ (63) at the measurement plane located 4 mm above the interface for (*c*) slow and (*d*) rapid ruptures. The exponential cohesive zone model at the interface is defined by two parameters, Γ and x_c. x_c is estimated from measurements of A in panel *a*. Γ was measured in **Figure 2**. Interface (*dashed lines*) and off-interface (*solid lines*) predictions of the cohesive zone model are also shown. Data taken from Reference 86.

and on-going effort is directed toward formulation of constitutive laws that endeavor to address these effects.

Direct measurements of the constitutive evolution law of friction are impeded by the singular nature of the fields. However, measurements of the real contact area, as performed in the reviewed experiments, shed light on how these singular fields are regularized, since these measurements, by definition, take place on the interface. **Figure 7*a*** demonstrates that $A(x,t)$ indeed decreases gradually behind the propagating rupture tip, in clear contrast to idealized singular cracks for which an abrupt reduction $A(x,t)$ is expected. The length scale over which $A(x,t)$ is reduced (63) provides an estimate of the cohesive zone size, x_c. **Figure 7*a*,*b*** demonstrates that x_c is not constant but systematically contracts with increasing C_f. It was shown (63) that this effective Lorenz contraction is predicted by LEFM (Equations 4 and 7) and is described by $x_c(C_f) = x_c(C_f = 0)/f_{II}(C_f, k)$, where $f_{II}(C_f, k)$ (note that $f_{II} \to 0$ as $C_f \to C_R$) is the same universal function that appears in Equation 4 (see **Figure 7*b***).

Knowledge of Γ and x_c, and the assumption of the simplest cohesive zone model, enable us to estimate elusive but long sought after constitutive parameters that characterize the dissipative processes and material properties at the extreme conditions that take place near the rupture tip. These include the peak shear strength τ_p (**Figure 7*c*,*d***, *top*), maximal slip velocity $2\dot{u}_x$ (**Figure 7*c*,*d***, *bottom*), and critical slip distance, d_c.

Figure 7 reveals that measurements performed slightly above the frictional interface do not reflect any of the cohesive zone dynamics or properties. This is especially true for $C_f \to C_R$, since $x_c \to 0$ in this regime. Measurements at finite distances from a frictional interface should, therefore, be interpreted with extreme caution as the divergence of the near-tip fields may result in erroneous conclusions. Credible measurements of the interface properties are particularly challenging as they can only be obtained if measurements are performed at distances from the rupture tip that are much smaller than x_c. It is progressively harder to meet this requirement as x_c contracts with the rupture velocity. Combined measurements of the real area of contact, slip, and stresses at the interface and their evolution is certainly an important research direction, if one would like to assess interface properties under friction.

3. CONCLUSIONS AND OPEN QUESTIONS

As demonstrated above, the transition from stick to slip is mediated by propagating rupture fronts. These ruptures couple dynamics at time and length scales that are separated by many orders of magnitude and determine whether macroscopic motion will ensue or not.

Although rupture fronts have long been considered to have much in common with propagating cracks, there had been little direct experimental evidence that quantitative universal predictions of LEFM really describe frictional failure. This brief review has summarized recent experimental results that have established the extensive applicability of brittle fracture theory to our understanding of both frictional rupture dynamics and to earthquake dynamics, an important but particular case. We have seen that the following is true:

- The elastic fields in the vicinity of both rapidly propagating and slow frictional rupture tips are extremely well described by the universal square-root singular solutions originally developed for brittle shear cracks.
- The singularity and dynamics of frictional ruptures are identical for both dry and boundary-lubricated interfaces.
- The singular fields provide a quantitative measure of the fracture energy, Γ, that is needed to advance a rupture.
- The dynamic behavior and arrest of frictional ruptures are entirely described by the classical fracture mechanics description of shear crack dynamics. Both have important implications for a fundamental understanding of earthquake dynamics. This simple description describes both extremely slow and rapid rupture fronts. The only physical quantities needed to differentiate between these extremes is the amount of elastic energy stored in the system prior to rupture nucleation and, of course, the distribution of the fracture energy along the interface.

The general simplicity and beauty of this approach should be emphasized. Once Γ, the sole free parameter that encapsulates the dissipative processes at the rupture tip, has been measured, rupture propagation, acceleration, and arrest are entirely predicted by its balance with the energy flux to the crack tip. This energy flux depends solely on the difference between the initial shear stress and the dynamic frictional resistance along the interface. Although a specific material (with both dry and boundary-lubricated interfaces) has been considered in this review, the results are general so long as several necessary conditions are satisfied. First, a small-scale yielding approximation should apply; a region in the rupture tips vicinity should exist where $\sigma \sim 1/\sqrt{r}$. Second, there should be no significant rate dependence of the frictional resistance within the rupture tail. This condition enables one to map the frictional interface to stress-free boundary conditions. Third, the particular analysis that we have used is valid for all times prior to the arrival of waves reflected from a sample's far boundaries back to the rupture tip. Once this occurs, fracture mechanics should

still describe rupture evolution, but a different (time-dependent) analysis of the singular fields will be necessary (see, e.g., References 137 and 138 for examples in tensile fracture).

Seismic inversions of earthquakes (139) and some laboratory experiments (140–142) have implied that ruptures may also be pulse-like, in which frictional slip ceases shortly behind the rupture front. This contrasts with the crack-like modes considered here, in which the slip velocity is not confined to a finite zone. Pulse-like behavior can occur when an interface is formed by two bodies with different elastic properties (59, 60) (forming a bimaterial interface) or for materials that undergo enhanced velocity weakening (stronger than logarithmic) at high slip rates (59, 119, 142–144). The form of the cohesive law governing the interface strength is quite important in this respect; for example, slip-weakening friction laws were unable to reproduce this rich phenomenology (142, 144). Whereas in PMMA slip-pulse modes haven't been observed, there is experimental evidence for slip-pulse modes in a different brittle plastic, Homalite (140–142). One key difference may be the behavior of the residual stress, τ_r, behind the rupture tip. In PMMA τ_r only mildly varies with the slip velocity (145), whereas in Homalite strong velocity weakening has been reported (66).

The propagation criterion outlined in Section 2.1 is a necessary condition for the onset of frictional motion. The onset of frictional motion, however, also requires rupture nucleation. We have shown that, once nucleation takes place, fracture mechanics will quantitatively describe ensuing rupture dynamics and/or arrest. However, it is unclear how to predict when and via what mechanisms nucleation will take place. For the Griffith criterion for rupture propagation to apply, for example, a singular seed crack must first exist. Understanding the spontaneous formation of such a seed crack from within a rough frictional interface is a fundamental question of great importance. Despite many interesting theoretical (7, 91, 146–153) and experimental (73, 154–156) efforts, it is still, however, not very well understood. From an experimental perspective there is a striking paucity of direct experimental observations of how nucleation takes place. Local measurements of stresses, slip, and contact area within the nucleation region and cohesive zone are very much needed.

DISCLOSURE STATEMENT

The authors are not aware of any affiliations, memberships, funding, or financial holdings that might be perceived as affecting the objectivity of this review.

ACKNOWLEDGMENTS

We acknowledge the support of both the US-Israel Binational Science Foundation (Grant No. 2016950), and Israel Science Foundation (Grant No. 1523/15).

LITERATURE CITED

1. Gnecco E, Bennewitz R, Gyalog T, Loppacher C, Bammerlin M, et al. 2000. *Phys. Rev. Lett.* 84:1172–75
2. Dienwiebel M, Verhoeven GS, Pradeep N, Frenken JWM, Heimberg JA, Zandbergen HW. 2004. *Phys. Rev. Lett.* 92:126101
3. Tian K, Gosvami NN, Goldsby DL, Liu Y, Szlufarska I, Carpick RW. 2017. *Phys. Rev. Lett.* 118:076103
4. Scholz C. 2002. *The Mechanics of Earthquakes and Faulting*. Cambridge: Cambridge Univ. Press. 2nd ed.
5. Ben-Zion Y. 2008. *Rev. Geophys.* 46:RG4006
6. Marone C. 1998. *Annu. Rev. Earth Planet. Sci.* 26:643–96
7. Ohnaka M. 2013. *The Physics of Rock Failure and Earthquakes*. New York: Cambridge Univ. Press. 1st ed.

8. Persson B. 2000. *Sliding Friction: Physical Principles and Applications*. Berlin, Heidelberg: Springer-Verlag. 2nd ed.
9. Fall A, Weber B, Pakpour M, Lenoir N, Shahidzadeh N, et al. 2014. *Phys. Rev. Lett.* 112:175502
10. Greenwood JA, Williamson JBP. 1966. *Proc. R. Soc. Lond. A: Math. Phys. Eng. Sci.* 295:300–19
11. Persson BNJ. 2001. *J. Chem. Phys.* 115:3840–61
12. Kogut L, Etsion I. 2002. *J. Appl. Mech.* 69:657–62
13. Paggi M, Ciavarella M. 2010. *Wear* 268:1020–29
14. Pastewka L, Robbins MO. 2014. *PNAS* 111:3298–303
15. Müser MH, Dapp WB, Bugnicourt R, Sainsot P, Lesaffre N, et al. 2017. *Tribol. Lett.* 65:118
16. Vakis A, Yastrebov V, Scheibert J, Minfray C, Nicola L, et al. 2018. *Tribol. Int.* 125:169–99
17. Aghababaei R, Warner DH, Molinari JF. 2016. *Nat. Commun.* 7:11816
18. Baumberger T, Caroli C. 2006. *Adv. Phys.* 55:279–348
19. Aharonov E, Scholz CH. 2018. *J. Geophys. Res.: Solid Earth* 123(2):1591–614
20. Rice JR, Lapusta N, Ranjith K. 2001. *J. Mech. Phys. Solids* 49:1865–98
21. Brener EA, Weikamp M, Spatschek R, Bar-Sinai Y, Bouchbinder E. 2016. *J. Mech. Phys. Solids* 89:149–73
22. Bowden FP, Tabor D. 2001. *The Friction and Lubrication of Solids*. New York: Oxford Univ. Press. 2nd ed.
23. Dieterich JH, Kilgore BD. 1996. *Tectonophysics* 256:219–39
24. Rabinowicz E. 1958. *Proc. Phys. Soc.* 71:668
25. Dieterich JH. 1979. *J. Geophys. Res.: Solid Earth* 84:2161–68
26. Ruina A. 1983. *J. Geophys. Res.: Solid Earth* 88:10359–70
27. Berthoud P, Baumberger T, G'Sell C, Hiver JM. 1999. *Phys. Rev. B* 59:14313–27
28. Baumberger T, Berthoud P, Caroli C. 1999. *Phys. Rev. B* 60:3928–39
29. Bar-Sinai Y, Spatschek R, Brener EA, Bouchbinder E. 2014. *J. Geophys. Res.: Solid Earth* 119:1738–48
30. Dieterich JH, Kilgore BD. 1994. *Pure Appl. Geophys.* 143:283–302
31. Ben-David O, Rubinstein SM, Fineberg J. 2010. *Nature* 463:76–79
32. Nagata K, Nakatani M, Yoshida S. 2012. *J. Geophys. Res.: Solid Earth* 117(B2):B02314
33. Dillavou S, Rubinstein S. 2018. *Phys. Rev. Lett.* 120:224101
34. Nakatani M. 2001. *J. Geophys. Res.: Solid Earth* 106:13347–80
35. Bhattacharya P, Rubin AM, Bayart E, Savage HM, Marone C. 2015. *J. Geophys. Res.: Solid Earth* 120:6365–85
36. Rice JR. 2006. *J. Geophys. Res.: Solid Earth* 111(B5):B05311
37. Goldsby DL, Tullis TE. 2011. *Science* 334:216–18
38. Passelègue FX, Goldsby DL, Fabbri O. 2014. *Geophys. Res. Lett.* 41:828–35
39. Reches Ze, Lockner DA. 2010. *Nature* 467:452–55
40. Chang JC, Lockner DA, Reches Z. 2012. *Science* 338:101–5
41. Goldsby DL, Tullis TE. 2002. *Geophys. Res. Lett.* 29(17):25–1–25–4
42. Brown KM, Fialko Y. 2012. *Nature* 488:638–41
43. Di Toro G, Han R, Hirose T, De Paola N, Nielsen S, et al. 2011. *Nature* 471:494–98
44. Rubinstein SM, Cohen G, Fineberg J. 2004. *Nature* 430:1005–9
45. Ben-David O, Fineberg J. 2011. *Phys. Rev. Lett.* 106:254301
46. Rabinowicz E. 1992. *Wear* 159:89–94
47. Brace WF, Byerlee JD. 1966. *Science* 153:990–92
48. Wu FT, Thomson KC, Kuenzler H. 1972. *Bull. Seismol. Soc. Am.* 62:1621–28
49. Johnson T, Wu FT, Scholz CH. 1973. *Science* 179:278–80
50. Johnson T, Scholz CH. 1976. *J. Geophys. Res.* 81:881–88
51. Okubo PG, Dieterich JH. 1984. *J. Geophys. Res.: Solid Earth* 89:5817–27
52. Freund LB. 1990. *Dynamic Fracture Mechanics*. New York: Cambridge Univ. Press
53. Broberg KB. 1999. *Cracks and Fracture*. San Diego: Academic
54. Fineberg J, Marder M. 1999. *Phys. Rep.-Rev. Sect. Phys. Lett.* 313:2–108
55. Palmer AC, Rice JR. 1973. *Proc. R. Soc. Lond. A: Math., Phys. Eng. Sci.* 332:527–48
56. Brener EA, Marchenko VI. 2002. *J. Exp. Theoret. Phys. Lett.* 76:211–14
57. Weertman J. 1980. *J. Geophys. Res.: Solid Earth* 85:1455–61

58. Xia K, Rosakis AJ, Kanamori H, Rice JR. 2005. *Science* 308:681–84
59. Ampuero J-P, Ben-Zion Y. 2008. *Geophys. J. Int.* 173:674–92
60. Shlomai H, Fineberg J. 2016. *Nat. Commun.* 7:11787
61. Aldam M, Bar-Sinai Y, Svetlizky I, Brener EA, Fineberg J, Bouchbinder E. 2016. *Phys. Rev. X* 6:041023
62. Rice JR. 1968. *J. Appl. Mech.* 35:379–86
63. Svetlizky I, Fineberg J. 2014. *Nature* 509:205–8
64. Bayart E, Svetlizky I, Fineberg J. 2016. *Phys. Rev. Lett.* 116:194301
65. Svetlizky I, Pino Muñoz D, Radiguet M, Kammer DS, Molinari JF, Fineberg J. 2016. *PNAS* 113:542–47
66. Rubino V, Rosakis AJ, Lapusta N. 2017. *Nat. Commun.* 8:15991
67. Okubo PG, Dieterich JH. 1981. *Geophys. Res. Lett.* 8:887–90
68. Ohnaka M, Kuwahara Y. 1990. *Tectonophysics* 175:197–220
69. McLaskey GC, Kilgore BD, Beeler NM. 2015. *Geophys. Res. Lett.* 42:7039–45
70. Xu S, Fukuyama E, Yamashita F, Mizoguchi K, Takizawa S, Kawakata H. 2018. *Tectonophysics* 733:209–31
71. Ohnaka M, Shen LF. 1999. *J. Geophys. Res.: Solid Earth* 104:817–44
72. Ben-David O, Cohen G, Fineberg J. 2010. *Science* 330:211–14
73. Nielsen S, Taddeucci J, Vinciguerra S. 2010. *Geophys. J. Int.* 180:697–702
74. Rosakis AJ, Samudrala O, Coker D. 1999. *Science* 284:1337–40
75. Xia K, Rosakis AJ, Kanamori H. 2004. *Science* 303:1859–61
76. Latour S, Gallot T, Catheline S, Voisin C, Renard F, et al. 2011. *Europhys. Lett.* 96:59003
77. Mello M, Bhat HS, Rosakis AJ. 2016. *J. Mech. Phys. Solids* 93:153–81
78. Xu S, Ben-Zion Y. 2017. *Geophys. J. Int.* 209:282
79. Passelègue FX, Schubnel A, Nielsen S, Bhat HS, Madariaga R. 2013. *Science* 340:1208–11
80. Trømborg J, Scheibert J, Amundsen DS, Thogersen K, Malthe-Sorenssen A. 2011. *Phys. Rev. Lett.* 107:074301
81. Kammer DS, Yastrebov VA, Spijker P, Molinari JF. 2012. *Tribol. Lett.* 48:27–32
82. Radiguet M, Kammer DS, Gillet P, Molinari JF. 2013. *Phys. Rev. Lett.* 111:164302
83. Trømborg JK, Sveinsson HA, Scheibert J, Thøgersen K, Amundsen DS, Malthe-Sørenssen A. 2014. *PNAS* 111:8764–69
84. Trømborg JK, Sveinsson HA, Thøgersen K, Scheibert J, Malthe-Sørenssen A. 2015. *Phys. Rev. E* 92:012408
85. Bar-Sinai Y, Brener EA, Bouchbinder E. 2012. *Geophys. Res. Lett.* 39:L03308
86. Svetlizky I, Kammer DS, Bayart E, Cohen G, Fineberg J. 2017. *Phys. Rev. Lett.* 118:125501
87. Freund LB. 1972. *J. Mech. Phys. Solids* 20:129–40
88. Freund LB. 1972. *J. Mech. Phys. Solids* 20:141–52
89. Peng Z, Gomberg J. 2010. *Nat. Geosci.* 3:599–607
90. Bouchbinder E, Brener EA, Barel I, Urbakh M. 2011. *Phys. Rev. Lett.* 107:235501
91. Bar-Sinai Y, Spatschek R, Brener EA, Bouchbinder E. 2013. *Phys. Rev. E* 88:060403
92. Kaproth BM, Marone C. 2013. *Science* 341:1229–32
93. Bayart E, Svetlizky I, Fineberg J. 2016. *Nat. Phys.* 12:166–70
94. Rubinstein SM, Cohen G, Fineberg J. 2007. *Phys. Rev. Lett.* 98:226103
95. Bayart E, Svetlizky I, Fineberg J. 2018. *J. Geophys. Res.: Solid Earth* 123(5):3828–48
96. Radiguet M, Kammer D, Molinari J. 2015. *Mech. Mater.* 80:276–87
97. Katano Y, Nakano K, Otsuki M, Matsukawa H. 2014. *Sci. Rep.* 4:6324
98. Maegawa S, Suzuki A, Nakano K. 2010. *Tribol. Lett.* 38:313–23
99. Taloni A, Benassi A, Sandfeld S, Zapperi S. 2015. *Sci. Rep.* 5:8086
100. Braun OM, Barel I, Urbakh M. 2009. *Phys. Rev. Lett.* 103:194301
101. Bar-Sinai Y, Spatschek R, Brener EA, Bouchbinder E. 2015. *Sci. Rep.* 5:7841
102. Kammer DS, Radiguet M, Ampuero J-P, Molinari JF. 2015. *Tribol. Lett.* 57:1–10
103. Olson EL, Allen RM. 2005. *Nature* 438:212
104. Ampuero J-P, Ripperger J, Mai PM. 2006. *Geophys. Monogr. Ser.*, Vol. 170, ed. R Abercrombie, A McGarr, G Di Toro, H Manamori, pp. 255–61. Washington, DC: Am. Geophys. Union
105. Galis M, Ampuero J-P, Mai PM, Cappa F. 2017. *Sci. Adv.* 3(12):eaap7528

106. Madariaga R. 1977. *Geophys. J. Int.* 51:625–51
107. Dunham EM. 2007. *J. Geophys. Res.: Solid Earth* 112(B7):B07302
108. Kostrov BV. 1975. *Int. J. Fracture* 11:47–56
109. Broberg KB. 1960. *Ark. Fys.* 18:159–92
110. Burridge R. 1973. *Geophys. J. R. Astron. Soc.* 35:439–55
111. Freund LB, Rosakis AJ. 1992. *J. Mech. Phys. Solids* 40:699–719
112. Andrews DJ. 1973. *Bull. Seismol. Soc. Am.* 63:1375–91
113. Bouchon M, Vallee M. 2003. *Science* 301:824–26
114. Dunham EM, Archuleta RJ. 2004. *Bull. Seismol. Soc. Am.* 94:S256–68
115. Abraham FF, Gao HJ. 2000. *Phys. Rev. Lett.* 84:3113–16
116. Geubelle PH, Kubair DV. 2001. *J. Mech. Phys. Solids* 49:571–87
117. Festa G, Vilotte JP. 2006. *Geophys. Res. Lett.* 33:L15320
118. Liu Y, Lapusta N. 2008. *J. Mech. Phys. Solids* 56:25–50
119. Gabriel AA, Ampuero J-P, Dalguer LA, Mai PM. 2012. *J. Geophys. Res.: Solid Earth* 117(B9):B09311
120. Liu C, Bizzarri A, Das S. 2014. *J. Geophys. Res.: Solid Earth* 119(11):8331–45
121. Psakhie SG, Shilko EV, Popov MV, Popov VL. 2015. *Phys. Rev. E* 91:063302
122. Bruhat L, Fang Z, Dunham EM. 2016. *J. Geophys. Res.: Solid Earth* 121(1):210–24
123. Barras F, Geubelle PH, Molinari JF. 2017. *Phys. Rev. Lett.* 119:144101
124. Albertini G, Kammer DS. 2017. *J. Geophys. Res.: Solid Earth* 122(8):6625–41
125. Barenblatt G. 1962. *Adv. Appl. Mech.* 7:55–129
126. Dugdale D. 1960. *J. Mech. Phys. Solids* 8:100–4
127. Ida Y. 1972. *J. Geophys. Res.* 77:3796
128. Andrews DJ. 1976. *J. Geophys. Res.: Solid Earth* 81:5679
129. Andrews DJ. 1985. *Bull. Seismol. Soc. Am.* 75:1–21
130. Bizzarri A, Cocco M, Andrews DJ, Boschi E. 2001. *Geophys. J. Int.* 144:656
131. Lu X, Lapusta N, Rosakis AJ. 2009. *Geophys. J. Int.* 177:717–32
132. Andrews DJ. 2005. *J. Geophys. Res.: Solid Earth* 110(B1):B01307
133. Andrews D. 2010. *Tectonophysics* 493:216–21
134. Weng H, Yang H. 2017. *Geophys. Res. Lett.* 44:2725–32
135. Poliakov ANB, Dmowska R, Rice JR. 2002. *J. Geophys. Res.: Solid Earth* 107(B11):2295
136. Samudrala O, Huang Y, Rosakis AJ. 2002. *J. Geophys. Res.-Solid Earth* 107(B8):2170
137. Marder M. 1991. *Phys. Rev. Lett.* 66:2484–87
138. Goldman T, Livne A, Fineberg J. 2010. *Phys. Rev. Lett.* 104:114301
139. Heaton TH. 1990. *Phys. Earth Planet. Inter.* 64:1–20
140. Lykotrafitis G, Rosakis AJ, Ravichandran G. 2006. *Science* 313:1765–68
141. Lu X, Lapusta N, Rosakis AJ. 2007. *PNAS* 104:18931–36
142. Lu X, Lapusta N, Rosakis AJ. 2010. *Int. J. Fract.* 163:27–39
143. Cochard A, Madariaga R. 1994. *Pure Appl. Geophys.* 142:419–45
144. Zheng G, Rice JR. 1998. *Bull. Seismol. Soc. Am.* 88:1466–83
145. Svetlizky I, Bayart E, Cohen G, Fineberg J. 2017. *Phys. Rev. Lett.* 118:234301
146. Dieterich JH. 1992. *Tectonophysics* 211:115–34
147. Ampuero J-P, Rubin AM. 2008. *J. Geophys. Res.: Solid Earth* 113(B1):B01302
148. Uenishi K, Rice JR. 2003. *J. Geophys. Res.: Solid Earth* 108(B1):2042
149. Rubin AM, Ampuero J-P. 2005. *J. Geophys. Res.: Solid Earth* 110(B11):B11312
150. Kaneko Y, Ampuero J-P. 2011. *Geophys. Res. Lett.* 38:L21307
151. Kaneko Y, Nielsen SB, Carpenter BM. 2016. *J. Geophys. Res.: Solid Earth* 121(8):6071–91
152. Viesca RC. 2016. *Proc. R. Soc. Lond. A: Math., Phys. Eng. Sci.* 472(2192): **https://doi.org/10.1098/rspa.2016.0254**
153. Aldam M, Weikamp M, Spatschek R, Brener EA, Bouchbinder E. 2017. *Geophys. Res. Lett.* 44:11,390–98
154. Latour S, Schubnel A, Nielsen S, Madariaga R, Vinciguerra S. 2013. *Geophys. Res. Lett.* 40:5064–69
155. McLaskey GC, Kilgore BD. 2013. *J. Geophys. Res.: Solid Earth* 118(6):2982–97
156. Fukuyama E, Tsuchida K, Kawakata H, Yamashita F, Mizoguchi K, Xu S. 2017. *Tectonophysics* 733:182–92